INSAR-BASED DETECTION AND MAPPING OF SEISMICALLY INDUCED GROUND SURFACE DISPLACEMENT AND DAMAGE IN PAMPANGA, PHILIPPINES

Enrico Luis Abcede[a], Abigail Ajesta[a], Jiriel Diego Alfonso[a], Ronn Joshua Nucup[a], Marielle Peralta[a], Ryan Ramirez[a,b]*

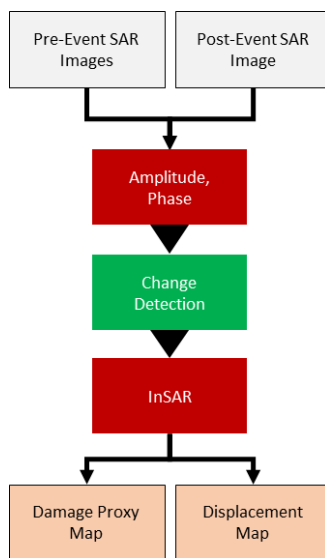[a]Department of Civil Engineering, University of Santo Tomas, España Boulevard, Sampaloc, Manila 1015, Philippines
[b]Division of Earth and Space Sciences, National Research Council of the Philippines, General Santos Avenue, Bicutan, Taguig 1631, Philippines

Graphical abstract

Abstract

On April 22, 2019, an earthquake with a magnitude M_w 6.1 struck the municipality of Castillejos in Zambales, the Philippines, and severely affected the province of Pampanga, which caused damage to commercial and residential structures reaching over 40 victims. This paper presents an approach for creating a pixel-based proxy damage assessment and displacement field maps to delineate the extent of ground surface displacements due to an earthquake. Specifically, this paper explored two change detection methods: the interferometric synthetic aperture radar (InSAR) technique and the coherence difference analysis method, using an open-source remote sensing software package and free SAR image data acquired by Sentinel-1 missions. Ground truth data were collected to substantiate the findings of the generated maps after the earthquake. Out of 7 surveyed damaged structures that were included in the National Disaster Risk Reduction and Management Council (NDRRMC) of the Philippines Situational Report, four damaged structures were successfully targeted using the proxy damage assessment map that had a coherence difference value ranging from 0.7-0.9 and damage grades of 3-5 based on the European Macroseismic Scale 1998 (EMS-98) damage classification system. This study confirms that change detection methods applied to C-band Sentinel-1 SAR data are valuable for mapping damaged areas and estimating ground surface displacements toward better hazard mitigation and disaster response.

Keywords: Sentinel-1 interferometric synthetic aperture radar, coherence difference, ground surface displacement, proxy damage assessment map, Zambales earthquake

1.0 INTRODUCTION

Frequent seismic and volcanic activities hit the Philippines, sitting along the Pacific Ring of Fire. The Philippine Institute of Volcanology and Seismology (PHIVOLCS) reported a powerful earthquake of magnitude M_w 6.1 in Zambales on April 22, 2019. The earthquake's epicenter was located on 14°59'N, 120°21'E (San Marcelino, Zambales), 18km east of Castillejos, with a focal depth of 20km. The Philippines' National Disaster Risk Reduction and Management Council (NDRRMC) confirmed 18 deaths, 3 people missing, and 256 injuries. The province of Pampanga suffered severe damage to 29 structures and was a devastated area by the earthquake. Pampanga sits on soft sediment and alluvial soil. This soil type risks undergoing liquefaction or fluidization in water-saturated unconsolidated sediments [1].

Detection and mapping of seismically induced ground surface displacement and assessing associated structural damages are crucial nowadays in the Philippines. In recent years, a new space-borne remote sensing technique was successfully applied to detect ground deformations due to natural hazards and identify hazard-induced disasters in urban and natural environments. Interferometric synthetic aperture radar (InSAR) [2, 3] is one of the popular remote sensing techniques which has been valuable for emergency response mitigation, disaster monitoring, and damage assessment in spatial and temporal dimensions. InSAR

has been used extensively for estimating earthquake-induced surface displacements [4, 5, 6, 7, 8, 9, 10]. InSAR can effectively provide rapid response maps for any disaster. InSAR and GPS observations investigated the static deformation of the 1999 M_w 7.1 Hector Mine earthquake in California [11]. In Taiwan, detection of damaged urban areas and measurement of earthquake-induced surface deformation due to the 1999 Chi-Chi earthquake were mapped and determined with ERS SAR images [12, 13]. In Iran, ENVISAT ASAR and ERS images were used to measure surface ruptures and map damage to buildings related to the 2003 earthquake that hit Bam [14, 15]. In Japan, ALOS PALSAR data was used to identify affected areas due to soil liquefaction [16] and ENVISAT ASAR data to estimate co-seismic and post-seismic deformations [17] due to the 2011 Tohoku earthquake. Decorrelation of ERS-1 SAR data was also used to detect urban damages in Kobe City, Japan, due to the 1995 Hyogoken-nanbu earthquake [18]. In Nepal, COSMO-SkyMed and ALOS PALSAR-2 images were used for InSAR coherence-change technique to detect damaged buildings due to the 2015 Gorkha earthquake [19]. The co-seismic coherence difference map in urban areas after the February 2016 Meinong earthquake in Taiwan was obtained using Sentinel-1 C-band radar interferometry [20]. In South Korea, a coherence change comparison before and after the November 2017 Pohang earthquake to detect liquefaction-affected areas was employed using Sentinel-1 SAR images [21].

Due to the complex processing of obtaining quality SAR images acquired from very long revisit periods and the high price of commercially available satellite images, minimal initiatives have utilized the coherence difference before and after earthquakes in the Philippines, even though the country frequently experiences natural hazards. With advances in geographical information systems (GIS), innovative remote sensing techniques through satellite earth observations for disaster management and mitigations have been achieved in recent years. The unprecedented availability of C-band Sentinel-1 SAR products under the Copernicus Programme of the European Space Agency (ESA) allowed many researchers in the remote sensing field to propose new algorithms and improve the existing ones to increase detection and monitoring capability and reliability using space-borne derived images.

This study employed the InSAR technique to detect and map the seismically induced ground surface displacement caused by the M_w 6.1 earthquake that severely hit the town of Porac, Pampanga, and adapted a change detection method to produce a proxy damage assessment map. The InSAR-derived maps would aid local and national government units to allocate relief resources and rescue operations effectively.

2.0 MATERIALS AND METHODS

2.1 Study Area

The M_w 6.1 Zambales earthquake produced intensities as high as Intensity VII, described by the PHIVOLCS Earthquake Intensity Scale. This powerful earthquake had caused liquefaction, landslides, and severe damage to well-built structures. PHIVOLCS reported that Mount Pinatubo, a stratovolcano in the Zambales Mountains near the epicentral region, did not show any anomalous activity that could trigger a possible eruption. One-thousand forty-nine aftershocks were reported on May 1, 2019, 16 of which were felt. A strike-slip mechanism characterized the fault plane, which had not been previously mapped. The strike, dip, and rake were 243.5°, 81.2°, and -174.4°, respectively.
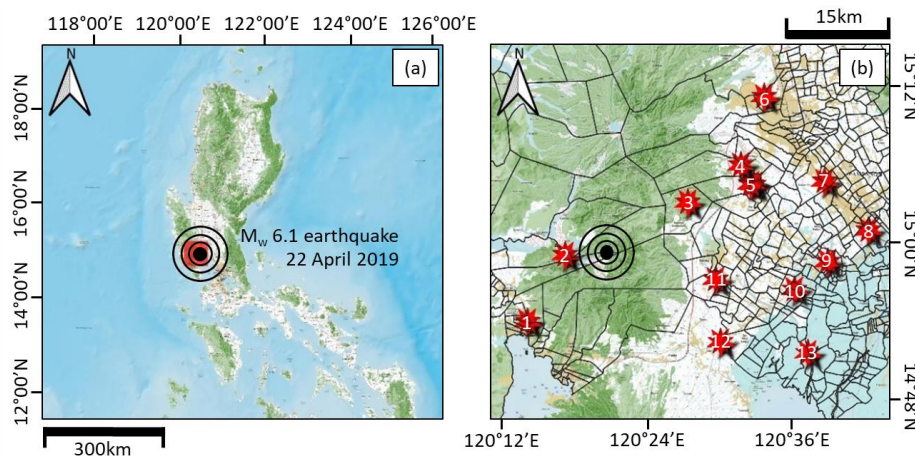
Figure 1 (a) The location of the study area in the Philippines and (b) the investigated area of interest (AOI) after the April 2019 Zambales earthquake

Figure 1 highlights the area of interest (AOI) investigated in this study, with red marks indicating damaged structures sampled from Situational Report No.15 from the NDRRMC dated May 3, 2019 [22]. Thirteen structures were selected that showed significant damage of Grade 2 or higher based on the European Macroseismic Scale 1998 (EMS-98) damage classification system [23], of which only seven were investigated that had factual evidence gathered from field surveys and online resources (news reports and articles). These structures included (i) the Consuelo Bridge, Floridablanca, (ii) Clark International Airport, (iii) Chuzon Supermarket, (iv) Porac Church, (v) Pampanga-Bataan Welcome Arc, (vi) San Agustin Parish Church, and (vii) Hacienda Dolores Church.

The area around Porac has tropopsamments with troporthents (arid unconsolidated sand deposits that contain no permanent weatherable minerals) and eutropepts with dystropepts (rich in organic matter) in Floridablanca and Castillejos, Zambales [24]. The AOI is mostly classified under

open/cultivated land. The nearest active fault is the Iba fault line which is some 30km from the epicenter and nearby areas that experienced damaged structures and is suggested to be the main fault that has caused the earthquake [25].

2.2 Basic Concept of InSAR

SAR is an imaging technique that utilizes microwaves of varying wavelengths [26]. SAR equipment can be on board aircraft or space-borne and take images of the earth's surface. These microwaves penetrate cloud cover and foliage and take elevation measurements through interferometry (InSAR). Each pixel in the SAR image contains amplitude and phase information. Phase, which is the distance between the sensor and the ground targets (also known as scatterers), measurements as a function of the satellite post and acquisition period permit the creation of digital elevation models (DEM) and estimation of centimetric to millimetric ground surface displacements of the earth's landscape.

The amplitude, which is the strength of the radar response, depends on the scatterers' roughness on the landscape. Typically, exposed rocks and built-up areas have higher amplitude than smooth flat surfaces that show low amplitude since the signal is mainly mirrored away from the sensor. The advantage of using a SAR image over an optical image is the use of the phase difference in any InSAR technique. Using optical imagery in the near nadir region challenges identifying damaged buildings with intact roof systems but experienced heavily damaged walls or cladding [27, 28]. Thus, using SAR datasets and the interferometric phase $\Delta\phi$, it is possible to detect damaged structures and infrastructures after a disastrous event.

However, many factors affect the phase difference. It is essential to isolate the temporal phase change to only see the displacement due to ground motion. As much as possible, $\Delta\phi$ must only contain the temporal phase change. This isolation can be done by applying other processing algorithms of InSAR. Equation (1) shows the factors that affect the phase change [29]:

$$\Delta\phi(P) = \Delta\varphi + \left(\frac{4\pi}{\lambda}\right)\Delta r + \Delta\alpha + \Delta v \qquad (1)$$

where the radar's image phase change value $\Delta\phi$ of a pixel P consists of four different phase contributions, namely: (i) $\Delta\varphi$ is the contribution to the phase due to the natural terrain and object that is being reflected (topographic information), (ii) $(4\pi/\lambda)\Delta r$ is the change in sensor-to-target distance, the phase contribution of interest for any InSAR analysis where we measure the surface change (displacement) of the target AOI, (iii) $\Delta\alpha$ is the atmospheric error contributions to the phase change, and (iv) Δv is the phase change contribution due to thermal noise and phase noise associated to some processing-induced factors. λ is the wavelength of the radar.

2.3 Datasets Used

36 Single-Look-Complex (SLC) images were gathered from the Alaska Satellite Facility in the Interferometric Wide (IW) swath mode from two satellite constellations, Sentinel-1A descending orbit (track 32) and Sentinel-1B ascending orbit (track 142). SLC images have a 5m × 20m spatial resolution in the range and azimuth directions, respectively, with the IW mode having a 250km swath width over its scanning area. Both satellites are right-side-looking with a C-band wavelength (λ = 5.6cm). Only the vertical-vertical (VV) polarization was used. A 24-day temporal baseline (TB) and a maximum of 150m perpendicular baseline (PB) were set for data selection to mitigate unstable scatter, leading to higher coherence and lesser background effects such as water vapor and ionospheric phase shifts.

Table 1 shows the list of satellite image pairs acquired and processed. Pair 1 of each scene contains the co-seismic pair, i.e., when the earthquake took place on April 22, 2019. The time format of each acquisition is yy/mm/dd. Pair 2 of each track contains the immediate pre-seismic pair or the image pair before the earthquake, while Pairs 3 through 17 are scenes over an entire year before the earthquake, which were used to average the phase and coherence for the removal of background effects. A pairing algorithm was used for the co-registration of the scenes. The pairing algorithm shown in Table 1 is called "master-switching", wherein consecutive pair dates are the master and slave image and was employed for the coherence change detection (CCD) sequence.

Table 1 Image pairing of the descending and ascending orbits

No.	Descending orbit (track 32)				Ascending orbit (track 142)			
	Master	Slave	TB (days)	PB (m)	Master	Slave	TB (days)	PB (m)
1	19/05/02	19/04/08	24	-111	19/05/04	19/04/10	24	36
2	19/04/08	19/03/15	24	-15	19/04/10	19/03/17	24	57
3	19/03/15	19/02/19	24	71	19/03/17	19/02/21	24	-84
4	19/02/19	19/01/26	24	9	19/02/21	19/01/28	24	31
5	19/01/26	19/01/02	24	-56	19/01/28	19/01/04	24	68
6	19/01/02	18/12/21	12	11	19/01/04	18/12/11	24	-48
7	18/12/21	18/11/27	24	-30	18/12/11	18/11/29	12	45
8	18/11/27	18/11/03	24	30	18/11/29	18/11/05	24	-16
9	18/11/03	18/10/10	24	16	18/11/05	18/10/12	24	-122
10	18/10/10	18/09/16	24	-14	18/10/12	18/09/18	24	28
11	18/09/16	18/08/23	24	-51	18/09/18	18/08/25	24	61
12	18/08/23	18/07/30	24	-25	18/08/25	18/08/01	24	-6
13	18/07/30	18/07/06	24	-11	18/08/01	18/07/08	24	-40
14	18/07/06	18/06/12	24	116	18/07/08	18/06/14	24	48
15	18/06/12	18/05/19	24	-53	18/06/14	18/05/21	24	-27
16	18/05/19	18/04/25	24	0	18/05/21	18/04/27	24	30
17	18/04/25	18/04/01	24	4	18/04/27	18/04/03	24	-62

2.4 Interferogram and Surface Displacement Formations

This section showcases the generation of the interferogram and the line-of-sight (LOS) surface displacement of the co-seismic pairs. (i) SLC scenes collected in the co-seismic pair were first split to focus over the target AOI, and their orbit-state vectors were imported to the image. (ii) This pair is co-registered with Bisinc 21-point interpolation in the DEM resampling method and resampling type. Interferogram formation and coherence estimation were simultaneously performed with a coherence range and azimuth window size of 5m × 5m. The scenes are then de-bursted to remove the black demarcated lines of the scene. (iii) The topographic contribution to the phase in the interferogram was then removed using the Shuttle Radar Topography Mission (SRTM) DEM 1 arcsec data (30m resolution). The multi-looking utility was employed with a 6m × 2m window to improve the image's visual quality at the cost of spatial resolution. The Goldstein phase filter [30] was then executed to decrease phase noise and was then exported to the SNAPHU program for phase unwrapping. (iv) The unwrapped phase was converted to LOS surface displacement. Masking out unrelated data (over the bodies of water) to the AOI and terrain correction were further applied. The LOS surface displacement of both scenes was then inverted to produce east-west and up-down displacements [31]. It must be noted that with the limitation of only having two satellite constellations, it is not possible to decompose the ground movement in three dimensions (up, east, and north components). However, due to the nature of the satellite trajectory being sun-synchronous (e.g., nearly polar orbit) and right-side looking, the phase measurements are more sensitive in the east-west direction than in the north, south direction. Hence, in this study, the contribution of the north-south movement component of the displacement field was ignored.

The InSAR measurements were utilized to investigate the ground surface displacements associated with different geohazards. The LOS displacement is the measurement of movements of the ground parallel to the direction of the path of the signal path. We first chose a reference point of high coherence for the co-seismic pair to measure all deformations at this point. This step is to mitigate any unstable measurements made. The relative displacement, $D^{re}(x_i, y_i)$, measured from a reference point, was evaluated as:

$$D^{re}(x_i, y_i) = D^{ab}(x_i, y_i) - K(x_i, y_i) \tag{2}$$

where $D^{ab}(x_i, y_i)$ is the actual LOS displacement obtained from InSAR, $K(x_i, y_i)$ is the offset measured from the actual LOS displacement at the reference point, and (x_i, y_i) are the latitude and longitude coordinates of the pixel being measured.

The east-west and up-down components of the relative displacement can be evaluated using the matrix formulation:

$$\begin{bmatrix} D^{re}_{asc}(x_i,y_i) \\ D^{re}_{desc}(x_i,y_i) \end{bmatrix} = \begin{bmatrix} S^u_{asc}(x_i,y_i) & S^e_{asc}(x_i,y_i) \\ S^u_{desc}(x_i,y_i) & S^e_{desc}(x_i,y_i) \end{bmatrix} \cdot \begin{bmatrix} D^{re}_u(x_i,y_i) \\ D^{re}_e(x_i,y_i) \end{bmatrix} \tag{3}$$

where $D^{re}_{asc}(x_i, y_i)$ and $D^{re}_{desc}(x_i, y_i)$ are the relative LOS displacement of both satellite constellations measured from the same reference point, S^u and S^e are the projection coefficients for both satellite constellations, and $D^{re}_u(x_i, y_i)$ and $D^{re}_e(x_i, y_i)$ are the relative surface displacement in the up-down and east-west component. The projection coefficients are evaluated as:

$$S^u(x_i, y_i) = \cos\theta(x_i, y_i)$$
$$S^e(x_i, y_i) = -\cos\alpha(x_i, y_i) \cdot \sin\theta(x_i, y_i) \tag{4}$$

where $\theta(x_i, y_i)$ and $\alpha(x_i, y_i)$ are the incidence and azimuth angles (measured clockwise from the north), respectively. These trajectory vectors are embedded in the metadata of each image acquisition.

To measure displacement fields due to ground movements of an earthquake, we assumed that the phase contributions of atmospheric errors are much smaller than the phase contribution by the earthquake event; therefore, the LOS displacement by the atmospheric errors was neglected. The interferogram, LOS, and inverted displacement fields were geocoded and illustrated in a GIS environment.

2.5 Proxy Damage Assessment Map Generation

We have employed the workflow developed by [16] and [20] to generate the proxy damage assessment map. The detected damaged structures were then compared to the EMS-98 damage classification system, and photographs of structures were presented.

During the interferogram generation, the coherence of each image scene was collected from both constellations, as presented in Table 1. The difference between pre- and co-seismic coherence image pairs was calculated as:

$$\Delta CI_u(x,y) = \gamma_{pre}(x,y) - \gamma_{co}(x,y) \tag{5}$$

where CI_u is the unnormalized coherence difference value, γ_{pre} is the pre-seismic coherence value, and γ_{co} is the co-seismic coherence value. Note that (x, y) is each pixel's range and azimuth coordinates. A filtering algorithm was employed to mitigate atmospheric effects that contributed to coherence difference uncertainty and expressed as:

$$\Delta\gamma_{threshold}(x,y) = \frac{1}{n}\sum_1^n \left(\gamma_{pre}(x,y) - \gamma_i(x,y)\right) + k\gamma_\sigma(x,y) \tag{6}$$
$$CI_u > \Delta\gamma_{threshold}(x,y) \cap CI_u \geq 0.5 \tag{7}$$

CI_u must first pass the first threshold $\Delta\gamma_{threshold}(x, y)$, computed in Equation (6). In this expression, the first term is the mean stack of the coherence differences of all pre-seismic coherence scenes on a per-pixel basis. The second term is the standard deviation of the differences of pre-seismic coherence scenes multiplied by a factor k. [11] suggests a k value of 3, assuming each pixel behaves within the normal distribution.

The second threshold was the natural coherence decay after 20 days, reaching a 0.5 value over forested/heavily vegetated areas [32]. Following [20], we used a second threshold that CI_u must be greater than or equal to 0.5, which is expressed in Equation (7). It was expected that areas used for farmland or vegetative cover would be filtered out to focus on detecting coherence change over built-up areas and removing any phase change due to atmospheric effects. The results are geocoded and visualized in a GIS environment. The workflow of the CCD algorithm is shown in Figure 2.
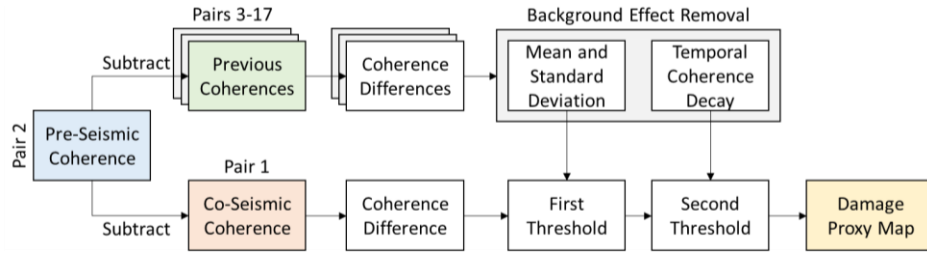
Figure 2 Coherence change detection (CCD) algorithm for the generation of proxy damage assessment map over Pampanga, the Philippines

The EMS-98 damage classification system, which was not presented in this study, was compared to the coherence difference value to determine the grades of the damaged structures investigated in the target AOI.

3.0 RESULTS AND DISCUSSION

3.1 Inversion of 2D Surface Displacement

Interferometry was performed on both ascending and descending scenes over the same AOI. The co-seismic interferogram and vertical and east-west displacement fields are shown in Figures 3-4, respectively. In Figure 3, interferometric fringes were hardly visible near the earthquake's epicenter (marked as a circled dot) due to the presence of vegetation. In Figure 4, an evident SW-NE strike-slip mechanism is shown with the blue and red areas of displacement. In Figure 4a, the red color variant corresponds to subsidence, and the blue color variant represents uplift. In Figure 4b, on the other hand, the red color variant indicates a westward movement, and the blue color variant corresponds to an eastward movement. The displacement components indicate more than 5cm ground movement over the AOI. However, it must be noted that the contribution to the displacement field has not been isolated to only account for temporal change, i.e., that any atmospheric errors have not been removed.
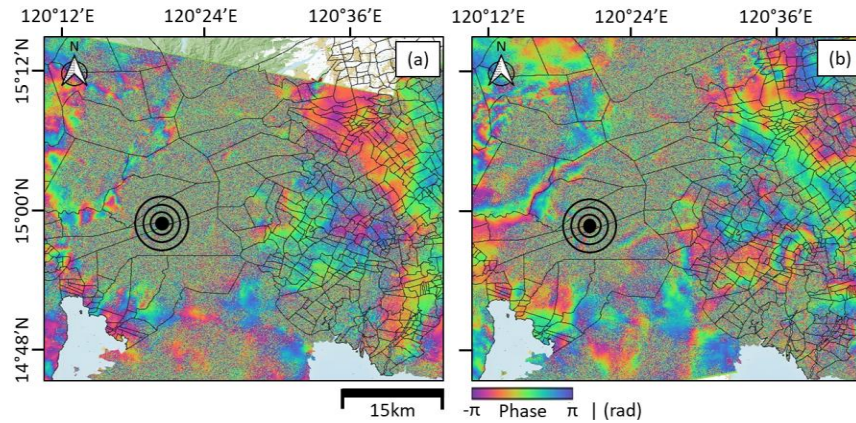

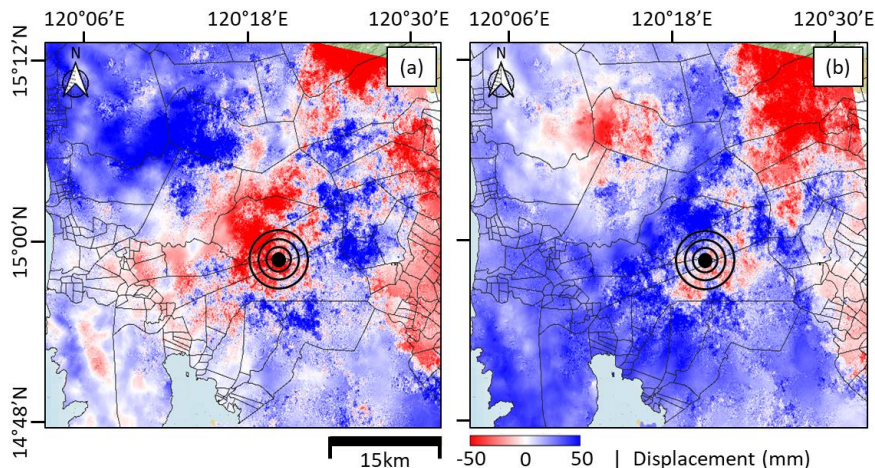**Figure 3** Co-seismic interferograms for (a) descending orbit and (b) ascending orbit

**Figure 4** (a) Vertical and (b) east-west displacement maps after inversion

3.2 Proxy Damage Assessment Map

Upon the formation of interferograms, coherence was estimated for each pair. A coherence value of 1, represented as warm colors, indicates a stable returned signal. A coherence value of 0, represented as cool colors, indicates an unstable returned signal. These values indicate a change in the coherence value over a target pixel since the path of the signal length has changed, indicating a phase shift and ultimately highlighting a movement of the surface which the signal had hit. High coherence values usually indicate built-up and urban areas, while low coherence values indicate vegetated areas. Table 2 shows the pertinent information about the pre- and co-seismic image pairs that were used to develop the coherence change detection results. The pairing algorithm keeps the temporal baseline equal to 24 days and the perpendicular baseline, not more than 150m.

Table 2 Information of pre-seismic and co-seismic image pairs

Figure	Track	Pair type	Master	Slave	TB (days)	PB (m)
5a	Descending	Pre-seismic	19/04/08	19/03/15	24	-15
5b	Descending	Co-seismic	19/05/02	19/04/08	24	-111
5d	Ascending	Pre-seismic	19/04/10	19/03/17	24	57
5e	Ascending	Co-seismic	19/05/04	19/04/10	24	36
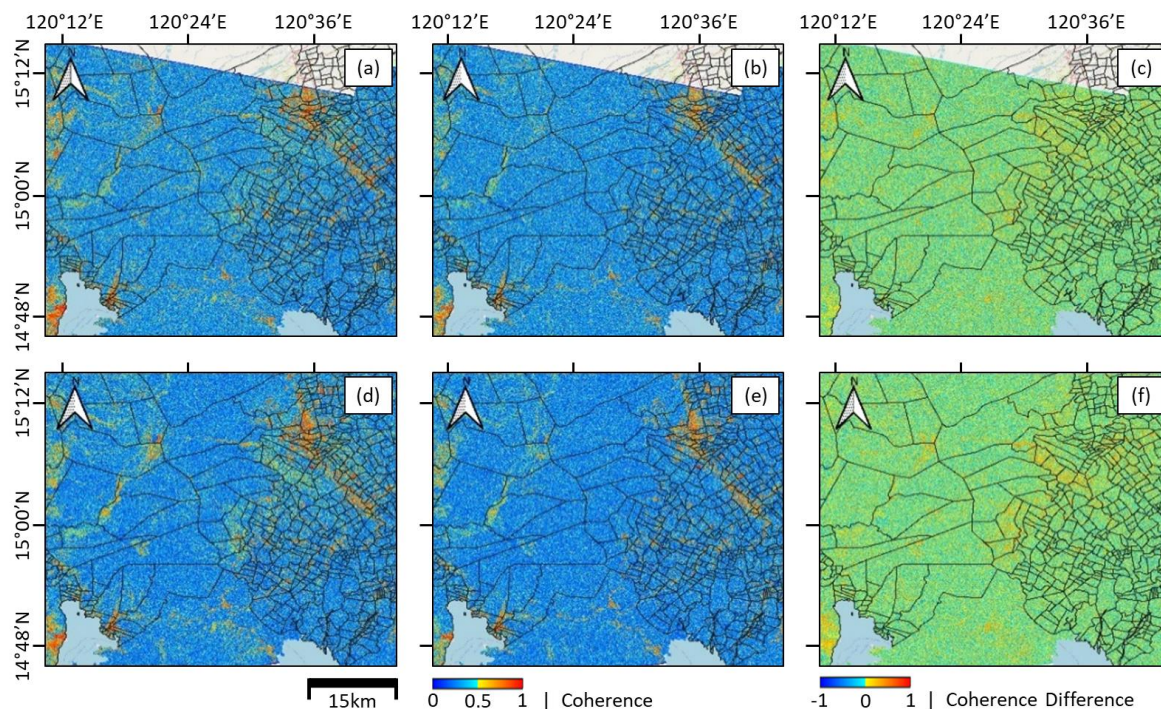
Figure 5 Coherence (a, b, d, e) and coherence difference (c, f) maps of both descending (a-c) and ascending (d-f) orbits

Coherence and coherence difference maps are shown in Figure 5. Figures 5a-c are for descending image pairs, while Figures 5d-f are for ascending image pairs. The coherence difference ranges from -1 (represented as cooler colors) to +1 (represented as warmer colors). Warmer regions indicate a decrease in coherence value and are a possible candidate for damage detection. Most coherence values were 0.2 to 0.3, indicating that most area is in vegetative regions. This result is consistent with the investigated AOI since many regions in Pampanga and Zambales are agricultural lands, which would create unstable backscatter in both imaging pairs from both scenes. The only reliable areas on hand are the built-up areas where damaged structures were detected. However, for the coherence differences, there is a possibility that the coherence values increased from the pre-seismic to the co-seismic region, which may be due to the changes in atmospheric delays in the phase change. These areas need to be filtered out to focus our target areas on damaged structures only.

Figure 6 emphasizes the severely affected town of Porac in Pampanga after the April 2019 Zambales earthquake. The collapsed Chuzon Supermarket and the Porac Church were examples of the effect of the coherence decrease and the evaluation of both scenes' coherence differences. As seen in Figure 6, the warm regions have decreased significantly from the pre-seismic pair to the co-seismic pair in both scenes over the AOI. The coherence difference maps highlight this decrease in warm regions (Figures 6c and 6f). However, there are also areas surrounding the warmer regions with cooler regions. It is counter-intuitive to see that the coherence would increase after an earthquake since we expect the signal to destabilize after an earthquake due to the ground surface displacement or building collapse, or at least have the same numerical values after the earthquake event. This observation is due to any phase error contributions such as atmospheric effects and water vapor contributions to phase change and is therefore imperative to be filtered out.
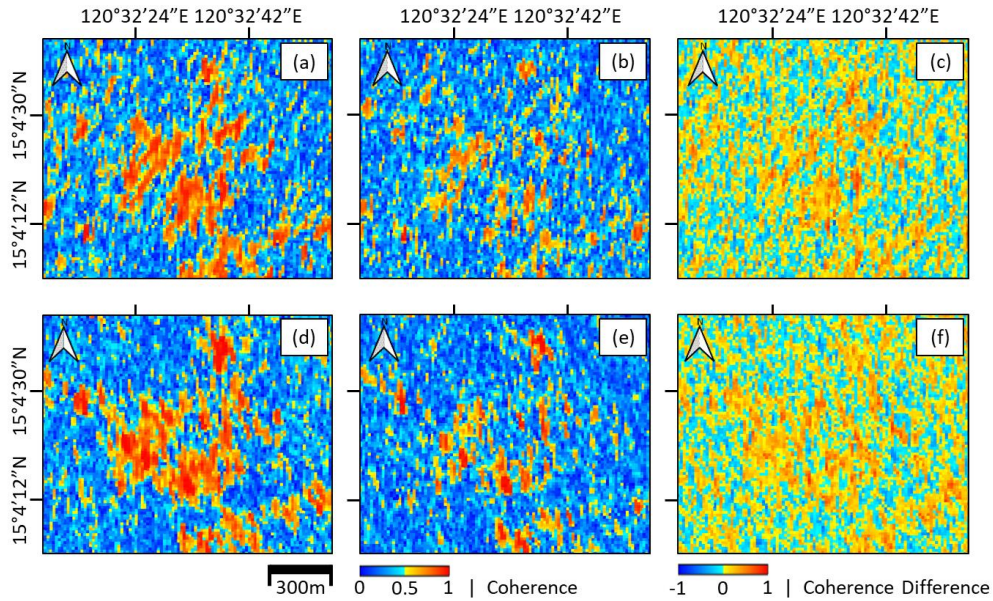
Figure 6 Coherence and coherence difference maps over the town of Porac, Pampanga from descending orbit (a-c) and ascending orbit (d-f)

Figure 7 illustrates the mean and standard deviations from descending and ascending orbits with similar results. The mean coherence difference shows the average coherence difference for each pixel, and the standard deviation showcases how often this deviates from the mean. Both scenes have mostly a standard deviation of about 0.15 while the mean maxes out mostly at zero coherence difference, suggesting that both scenes have most of their pixel points in stable condition over the entire stack of images. There was a relatively stable coherence value spatial distribution before the 2019 Zambales earthquake, which can be utilized to mitigate background effects.
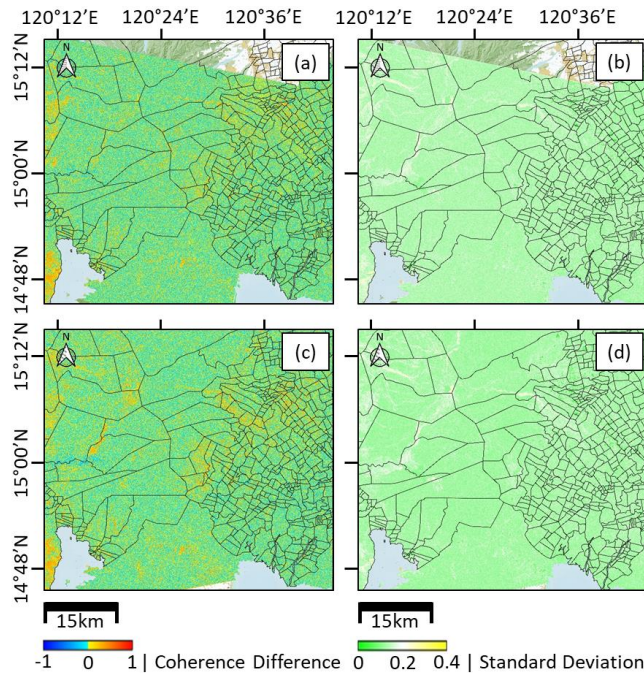

Figure 7 The mean (a and c) and the standard deviation (b and d) of coherence difference stack images for descending orbit (a-b) and ascending orbit (c-d)

Figure 8 clearly shows that the proxy damage assessment map has well captured the buildings reported to be damaged (Porac Church and Chuzon Supermarket). Other areas within the locality have been highlighted for potential damage, but with limited evidence gathered, these areas cannot be verified, so the focus was kept on these two structures. The coherence difference of both structures has been measured at 0.7 with a damage grade of 4 for the Porac Church and 5 for the Chuzon Supermarket based on EMS-98. Figure 9 shows the Consuelo Bridge in Floridablanca, Pampanga, to have a ruptured bridge

roadway. The coherence difference analysis method has highlighted the damaged bridge. The bridge damage grade can be classified as a grade 3 based on EMS-98.
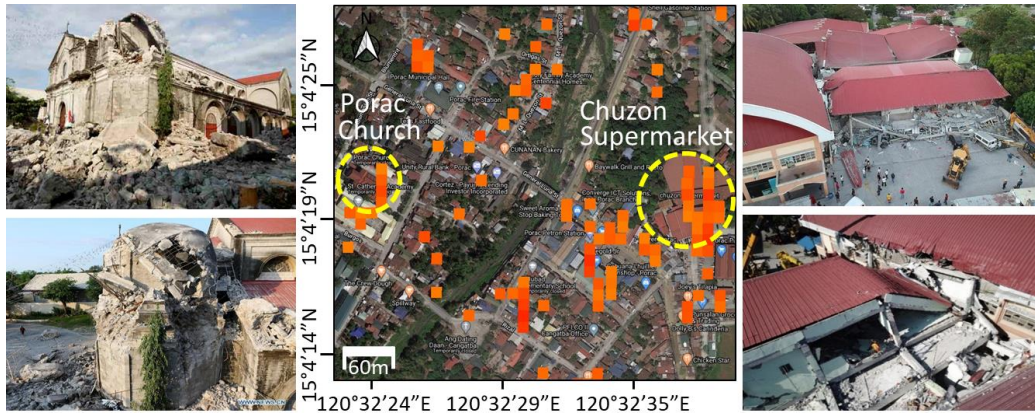

Figure 8 The proxy damage assessment map over Porac, Pampanga highlighting the targeted damaged Porac Church and Chuzon Supermarket (Source: www.news.cn, www.tempo.com.ph, and www.gmanetwork.com)
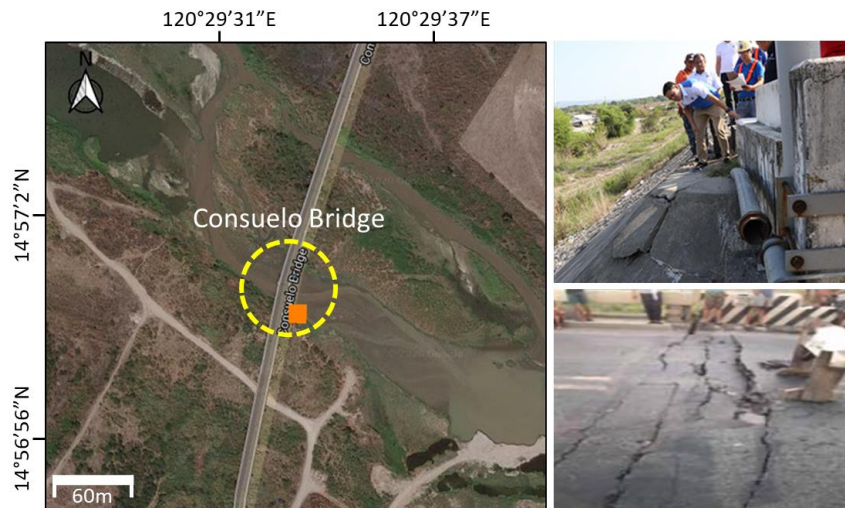

Figure 9 The proxy damage assessment map over Floridablanca, Pampanga highlighting the targeted damaged Consuelo Bridge (Source: www.rappler.com and ph.news.yahoo.com)
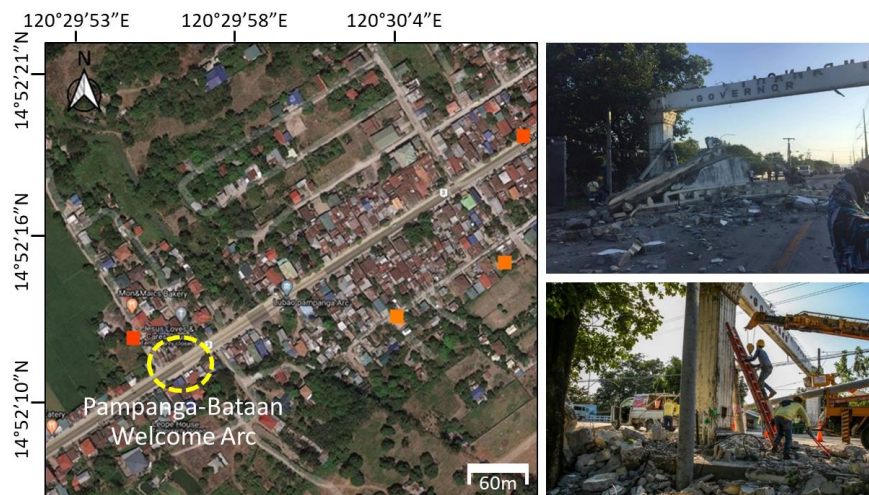

Figure 10 The proxy damage assessment map over Lubao, Pampanga highlighting the limitation of the proxy damage assessment map in targeting small, damaged structures such as the Pampanga-Bataan Welcome Arc (Source: news.abs-cbn.com)

Figure 10 shows the damaged welcome arc of Pampanga and Bataan in Lubao, Pampanga. In this case, the composited proxy damage assessment map did not highlight the damaged structure. This observation may be explained due to the limited spatial resolution of the image acquisition of the satellite to be 20m × 5m in the azimuth and range directions and the coherence window size set to a regular grid at 5m × 5m, resulting in a final spatial resolution of 100m × 25m. If a structure is smaller than this spatial resolution, the map may not be able to identify the damaged structure. This spatial feature is noted to be a limitation of the CCD algorithm. EMS-98 damage classification is seen to be at a grade of 2 for this structure. Table 3 summarizes the findings from the proxy damage assessment map.

Table 3 Summary of proxy damage assessment map findings

Structure	Coherence difference value	CCD algorithm	EMS 98 damage classification grade
Consuelo Bridge	0.7	Yes	3 (Concrete)
Clark International Airport	0.7	Yes	3 (Concrete)
Chuzon Supermarket	0.7-0.9	Yes	5 (Concrete)
Porac Church	0.7-0.9	Yes	4 (Masonry)
Pampanga-Bataan Welcome Arc	N/A	No	2 (Concrete)
San Agustin Parish Church	N/A	No	2 (Masonry)
Hacienda Dolores Church	N/A	No	2 (Masonry)

4.0 CONCLUSION

This paper outlines the general workflow when studying earthquake events in the Philippines by utilizing different change detection methods under remote sensing–InSAR and coherence difference analyses. For April 22, 2019, Zambales earthquake, which was a timely case study for these methodologies, the following findings are submitted: (i) Vertical and east-west displacement components' measurements on the co-seismic scene after the inversion of the interferometric results were estimated at a maximum of ±5cm near the epicenter of the earthquake. A strike-slip fault mechanism was observed based on the displacement field near the epicenter. However, it is unclear whether the Iba or East Zambales fault has triggered this earthquake event or any of the other fault lines that have not been demarcated as part of the Philippine fault system. There are high variations of vertical and east-west surface displacements for areas where damaged structures were investigated. (ii) The coherence change detection module has been shown to produce spatially accurate damage detection of grades 3 and higher when compared to the EMS-98 damage classification system. 4 out of 7 sampled damaged structures were detected, which registered from 0.7-0.9 in the coherence difference. This observation suggests a range where damage can be detected. The limitation, however, is that the area of damage should be greater than the spatial resolution of the return signal; otherwise, the CCD algorithm will not be able to detect the damaged structure. Nevertheless, the change detection methods employed gave reasonably good results in generating a proxy damage assessment map in a wide field of view for assessing the effects of the earthquake for a quick response in reconnaissance and rescue operations.

Acknowledgement

References

[1]   Topal, S., and Özkul, M. 2014. Soft-sediment Deformation Structures Interpreted as Seismites in the Kolankaya Formation, Denizli Basin (SW Turkey). *The Scientific World Journal*. 2014: 352654. DOI: https://doi.org/10.1155/2014/352654

[2]   Bürgmann, R., Rosen, P.A., and Fielding, E.J. 2000. Synthetic Aperture Radar Interferometry to Measure Earth's Surface Topography and Its Deformation. *Annual Review of Earth and Planetary Sciences*. 28: 169-209. DOI: https://doi.org/10.1146/annurev.earth.28.1.169

[3]   Fernández, J., Romero, R., Carrasco, D., Luzón, F., and Araña, V. 2002. InSAR Volcano and Seismic Monitoring in Spain. Results for the Period 1992-2000 and Possible Interpretations. *Optics and Lasers in Engineering*. 37(2-3): 285-297. DOI: https://doi.org/10.1016/S0143-8166(01)00085-9

[4]   Zebker, H.A., Rosen, P.A., Goldstein, R.M., Gabriel, A., and Werner, C.L. 1994. On the Derivation of Coseismic Displacement Fields using Differential Radar Interferometry: The Landers Earthquake. *Journal of Geophysical Research: Solid Earth*. 99(B10): 19617-19634. DOI: https://doi.org/10.1029/94JB01179

[5]   Wright, T., Fielding, E.J., and Parsons, B. 2001. Triggered Slip: Observations of the 17 August 1999 Izmit (Turkey) Earthquake using Radar Interferometry. *Geophysical Research Letters*. 28(6): 1079-1082. DOI : https://doi.org/10.1029/2000GL011776

[6]   Kuang, J., Ge, L., Metternicht, G.I., Ng, A.H.M., Wang, H., Zare, M., and Kamranzad, F. 2019. Coseismic Deformation and Source Model of the 12 November 2017 Mw 7.3 Kermanshah Earthquake (Iran-Iraq Border) Investigated through DInSAR Measurements. *International Journal of Remote Sensing*. 40(2): 532-554. DOI: https://doi.org/10.1080/01431161.2018.1514542

[7]   Ramdani, F., Setiani, P., and Setiawati, D.A. 2019. Analysis of Sequence Earthquake of Lombok Island, Indonesia. *Progress in Disaster Science*. 4: 100046. DOI : https://doi.org/10.1016/j.pdisas.2019.100046

[8]   Canaslan Çomut, F., Gürboğa, Ş., and Smail, T. 2020. Estimation of Co-seismic Land Deformation due to Mw 7.3 Earthquake in Iran (12 November 2017) using Sentinel-1 DInSAR. *Bulletin of the Mineral Research and Exploration*. 162(162): 11-30. DOI: https://doi.org/10.19111/bulletinofmre.604026

[9]   Suresh, D., and Yarrakula, K. 2020. InSAR based Deformation Mapping of Earthquake using Sentinel 1A Imagery. *Geocarto International*.

35(5): 559-568. DOI: https://doi.org/10.1080/10106049.2018.1544289

[10]   Bayik, C. 2021. Deformation Analysis of 2020 mw 5.7 Karlıova, Turkey, Earthquake using DInSAR Method with Different Incidence Angle SAR Data. *Arabian Journal of Geosciences*. 14: 273. DOI: https://doi.org/10.1007/s12517-021-06670-x

[11]   Simons, M., Fialko, Y., and Rivera, L. 2002. Coseismic Deformation from the 1999 Mw 7.1 Hector Mine, California, Earthquake as Inferred from InSAR and GPS Observations. *Bulletin of the Seismological Society of America*. 92(4): 1390-1402. DOI: https://doi.org/10.1785/0120000933

[12]   Chang, C.P., Wang, C.T., Chang, T.Y., Chen, K.S., Liang, L.S., Pathier, E., and Angelier, J. 2004. Application of SAR Interferometry to a Large Thrust Deformation: The 1999 Mw = 7.6 Chichi Earthquake in Central Taiwan. *Geophysical Journal International*. 159(1): 9-16. DOI: https://doi.org/10.1111/j.1365-246X.2004.02385.x

[13]   Yen, J.Y., Chen, K.S., Chang, C.P., and Ng, S.M. 2006. Deformation and "Deformation Quiescence" prior to the Chi-Chi Earthquake Evidenced by DInSAR and Groundwater Records during 1995-2002 in Central Taiwan. *Earth, Planets and Space*. 58: 805-813. DOI: https://doi.org/10.1186/BF03351985

[14]   Fielding, E.J., Talebian, M., Rosen, P.A., Nazari, H., Jackson, J.A., Ghorashi, M., and Walker, R. 2005. Surface Ruptures and Building Damage of the 2003 Bam, Iran, Earthquake Mapped by Satellite Synthetic Aperture Radar Interferometric Correlation. *Journal of Geophysical Research: Solid Earth*, 110(B3): 1-15. DOI: https://doi.org/10.1029/2004JB003299

[15]   Matsuoka, M., and Yamazaki, F. 2005. Building Damage Mapping of the 2003 Bam, Iran, Earthquake using Envisat/ASAR Intensity Imagery. *Earthquake Spectra*. 21(1): 285-294. DOI: https://doi.org/10.1193%2F1.2101027

[16]   Ishitsuka, K., Tsuji, T., and Matsuoka, T. 2012. Detection and Mapping of Soil Liquefaction in the 2011 Tohoku Earthquake using SAR Interferometry. *Earth, Planets and Space*. 64: 1267-1276. DOI: https://doi.org/10.5047/eps.2012.11.002

[17]   ElGharbawi, T., and Tamura, M. 2015. Coseismic and Postseismic Deformation Estimation of the 2011 Tohoku Earthquake in Kanto Region, Japan, using InSAR Time Series Analysis and GPS," *Remote Sensing of Environment*. 168: 374-387. DOI: https://doi.org/10.1016/j.rse.2015.07.016

[18]   Yonezawa, C., and Takeuchi, S. 2001. Decorrelation of SAR Data by Urban Damages caused by the 1995 Hyogoken-nanbu Earthquake. *International Journal of Remote Sensing*. 22(8): 1585-1600. DOI: https://doi.org/10.1080/01431160118187

[19]   Yun, S.H., Hudnut, K., Owen, S., Webb, F., Simons, M., Sacco, P., Gurrola, E., Manipon, G., Liang, C., and Fielding, E.J. 2015. Rapid Damage Mapping for the 2015 Mw 7.8 Gorkha Earthquake using Synthetic Aperture Radar Data from COSMO-SkyMed and ALOS-2 Satellites. *Seismological Research Letters*. 86(6): 1549-1556. DOI: https://doi.org/10.1785/0220150152

[20]   Lu, C.H., Ni, C.F., Chang, C.P., Yen, J.Y., and Chuang, R.Y. 2018. Coherence Difference Analysis of Sentinel-1 SAR Interferograms to Identify Earthquake-induced Disasters in Urban Areas. *Remote Sensing*. 10(8): 1318. DOI: https://doi.org/10.3390/rs10081318

[21]   Baik, H., Son, Y.S., and Kim, K.E. 2019. Detection of Liquefaction Phenomena from the 2017 Pohang (Korea) Earthquake using Remote Sensing Data. *Remote Sensing*. 11(18): 2184. DOI: https://doi.org/10.3390/rs11182184

[22]   Jalad, R. 2019. Situational Report No. 15 re Magnitude 6.1 Earthquake in Castillejos, Zambales, National Disaster Risk Reduction Management Council, Philippines.

[23]   Grünthal, G. 1998. European Macroseismic Scale 1998, Conseil de l'Europe–Cahiers du Centre Européen de Géodynamique et de Séismologie, 15. Editor G. Grünthal, Luxembourg.

[24]   Soil Map of Region III (1st ed.), 1988. Department of Environment and Natural Resources:

[25]   Distribution of Active Faults in Region III. 2019. Philippine Institute of Volcanology and Seismology:

[26]   Ferretti, A., Monti-Guarnieri, A., Prati, C., Rocca, F., and Massonnet, D. 2007. InSAR Principles: Guidelines for SAR Interferometry Processing and Interpretation, ESA Publications.

[27]   Dell'Acqua, F., and Gamba, P. 2012. Remote Sensing and Earthquake Damage Assessment: Experiences, Limits, and Perspectives. *Proceedings of the IEEE*. 100(10): 2876-2890. DOI: https://doi.org/10.1109/JPROC.2012.2196404

[28]   Voigt, S., Schneiderhan, T., Twele, A., Gähler, M., Stein, E., and Mehl, H. 2011. Rapid Damage Assessment and Situation Mapping: Learning from the 2010 Haiti Earthquake. *Photogrammetric Engineering & Remote Sensing*. 77(9): 923-931. DOI: https://doi.org/10.14358/PERS.77.9.923

[29]   Ferretti, A. 2014. Satellite InSAR Data: Reservoir Monitoring from Space, European Association of Geoscientists & Engineers (EAGE), The Netherlands.

[30]   Goldstein, R.M., and Werner, C.L. 1998. Radar Interferogram Filtering for Geophysical Applications. *Geophysical Research Letters*. 25(21): 4035-4038. DOI: https://doi.org/10.1029/1998GL900033

[31]   Yu, X., Hu, J., and Sun, Q. 2017. Estimating Actual 2D Ground Deformations Induced by Underground Activities with Cross-heading InSAR Measurements. *Journal of Sensors*. 2017: 3170506. DOI: https://doi.org/10.1155/2017/3170506

[32]   Zebker, H.A., and Villasenor, J. 1992. Decorrelation in Interferometric Radar Echoes. *IEEE Transactions on Geoscience and Remote Sensing*. 30(5): 950-959. DOI: https://doi.org/10.1109/36.175330